($t = 392$ μs) when the viscous effects are accounted for (see Fig. 5b). This is because viscous effects can be thought of as a mechanism that introduces suction into the flowfield along the wall. Consequently, the amount of fluid trapped under the bifurcated shock is smaller when viscous effects are accounted for. It is also important to note that although in an inviscid case (Fig. 5a), a clear stagnation point is evident behind the vortex, in the viscous case (Fig. 5b), a clear boundary layer is seen to develop along the wall behind the vortex.

It is also evident from Figs. 5a and 5b that although the precursor precedes the shock wave by about 7.8 cm when the fluid is assumed to be inviscid, the precursor is only 4.3 cm ahead of the shock wave for the viscous case.

The stagnation point, on the other hand, lags about 5 and 4.2 cm behind the shock wave in the inviscid and viscous cases, respectively.

The dependence of the triple-point trajectory on the densities ratio ρ_4/ρ_1 for both viscous and inviscid fluids is shown in Fig. 6 for a fixed shock wave Mach number $M_s = 2$.

Figure 6 indicates the following:

1) For an inviscid fluid, the triple-point trajectory is a straight line.

2) For a viscous fluid, the triple-point trajectory approaches a constant height.

3) The triple point is higher when the fluid is assumed to be inviscid.

4) The smaller ρ_4/ρ_1 is, the higher the triple-point height. Recall that since $P_4 = P_1$, i.e., $P_4/P_1 = 1$, $T_1/T_4 = \rho_4/\rho_1$, smaller values of ρ_4/ρ_1 are equivalent to larger values of T_4/T_1, i.e., higher temperatures inside the thermal layer.

The dependence of the triple-point trajectory on the shock wave Mach number M_s for both viscous and inviscid fluids is shown in Fig. 7 for a fixed value of $\rho_4/\rho_1 = 0.2$. It is again evident that the triple-point trajectories are straight when the fluid is assumed to be inviscid. However, when viscosity is accounted for, then the triple-point trajectories approach an asymptotic level.

The pressure distributions along the surface for an inviscid and a viscous case are shown in Figs. 8 and 9, respectively. The maximum pressure along the surface is obtained at the stagnation point behind the shock wave. As shown in Fig. 8, the stagnation pressure increases from about $P_{4st} = 4.69\ P_1$ at $\tau = 3.7$ ($t = 125.8$ μs) to about $P_{4st} = 5.24\ P_1$ at $\tau = 7.4$ ($t = 251.6$ μs) and finally to about $P_{4st} = 5.37\ P_1$ at $\tau = 11.1$ ($t = 377.4$ μs). This trend might suggest that the stagnation pressure approaches an asymptotic value.

When viscous effects are accounted for (see Fig. 9), the stagnation pressure increases from about $P_{4st} = 5.10\ P_1$ at $\tau = 12.41$ ($t = 421.9$ μs) to about $P_{4st} = 5.29\ P_1$ at $\tau = 16.55$ ($t = 562.7$ μs) and finally to about $P_{4st} = 5.41\ P_1$ at $\tau = 20.70$ ($t = 703.8$ μs). Unlike the case of an inviscid fluid, it cannot be concluded from these values that an asymptotic stagnation pressure is approached. This is in spite of the fact that the viscous calculations shown in Fig. 9 extend to 703.8 μs after the interaction started, whereas the inviscid calculations shown in Fig. 8 extend only to 377.4 μs.

Note that Figs. 8 and 9 imply that the so-called stagnation point moves along the surface in the x direction. The horizontal velocity of the stagnation point seems to be larger when the fluid is assumed to be inviscid.

Furthermore, although for both the viscous and the inviscid calculations the horizontal velocity of the stagnation point seems to be constant, the horizontal velocity of the leading edge of the precursor seems to be increasing, i.e., the leading edge of the precursor seems to be accelerating. Note in Fig. 8 that although in the first time interval of $\Delta\tau = 3.7$ ($\Delta t = 125.8$ μs) the precursor propagated a distance of 1.18 cm, in the second time interval of $\Delta\tau = 3.7$, the precursor advanced about 1.49 cm, i.e., its average velocity increased about 26%. Similarly, for the viscous case (Fig. 9) in the first time interval of $\Delta\tau = 4.14$ ($\Delta t = 140.76$ μs) the precursor propagated about 0.625 cm, whereas in the second time interval of $\Delta\tau = 4.15$ ($\Delta t = 141.1$ μs), it propagated a distance of about 0.729 cm. This difference implies an increase of about 16% in the average velocity of the precursor.

Acknowledgment

The authors would like to thank the Pearlstone Center for Aeronautical Engineering Studies for financially supporting D. Rayevsky's stay in the Department of Mechanical Engineering of the Ben-Gurion University of the Negev.

References

[1]Hess, R. V., "Interaction of Moving Shocks and Hot Layers," NACA TN 4002, 1957.

[2]Griffith, W. C., "Interaction of a Shock Wave with a Thermal Boundary Layer," *Journal of Aeronautical Sciences,* Vol. 23, No. 1, 1956 pp. 16-22.

[3]Gion, E. J., "Plane Shock Interacting with Thermal Layer," *Physics of Fluids,* Vol. 20, No. 4, 1977, pp. 700-702.

[4]Reichenbach, H., "Roughness and Heated Layer Effects on Shock Wave Propagation and Reflection—Experimental Results," Ernst Mach Inst., Freiburg, Germany, Rept. E24/85, 1985.

[5]Schneyer, G. P., and Wilkins, D. E., "Thermal Layer-Shock Interaction (Precursor) Simulation Data Book," S-Cubed, Rept. SSS-R-84-6584, Albuquerque, NM, 1984.

[6]Glowacki, W. S., Kuhl, A. L., Glaz, H. M., and Ferguson, R. E., "Shock Wave Interaction with High Sound Speed Layers," *Shock Waves and Shock Tubes,* edited by D. Bershader and R. Hanson, Stanford Univ. Press, Berkeley, CA, 1986, pp. 187-194.

[7]Fry, M., and Book, D. L., "Shock Dynamics in Heated Layers," *Shock Waves and Shock Tubes,* edited by D. Bershader and R. Hanson, Stanford Univ. Press, Berkeley, CA, 1986, pp. 517-522.

[8]Mirels, H., "Interaction of Moving Shock with Thin Stationary Thermal Layer," *Shock Tubes and Waves,* edited by H. Gronig, VCH, Weinheim, Germany, 1988, pp. 177-183.

[9]Shokin, Yu. I., *A Method of Differential Approximation,* Novosibirsk, Nauke, Russia, 1979 (in Russian).

[10]Lyakhov, V. N., private communication, 1990.

[11]MacCormack, R. W., "The Effect of Viscosity on Hypervelocity Impact Cratering," AIAA Paper 69-354, 1969.

[12]Boris, J., and Book, D., "Flux-Corrected Transport: I SHASTA, A Fluid Transport Algorithm that Works," *Journal of Computational Physics,* Vol. 11, 1973, pp. 38-44.

Frequency Analysis of Axially Loaded Structures

C. Sundararajan*
Houston, Texas 77396

Introduction

NATURAL frequencies of axially loaded beams, plates, shells, and other types of components are often required in the design of aerospace structures. Changes in the location of masses such as instruments, equipment, and other attachments that add to the mass of structures without contributing significantly to structural stiffness do affect the natural frequencies. Axial loads, if sufficiently high, also affect the natural frequencies. Hence, design engineers are interested in the effect of alterations in mass distributions and axial loads on the natural frequencies in order to obtain optimal or near-optimal structural design by using an ideal combination of mass distribution and axial load. Repeated frequency analyses of the structure with various combinations of mass distributions and axial loads is an expensive and time-consuming process. If, however, a simple procedure were available to study the

Received Aug. 29, 1989; revision received Feb. 17, 1990; accepted for publication March 6, 1990.

*Consultant, 10723 Thorncliff Drive.

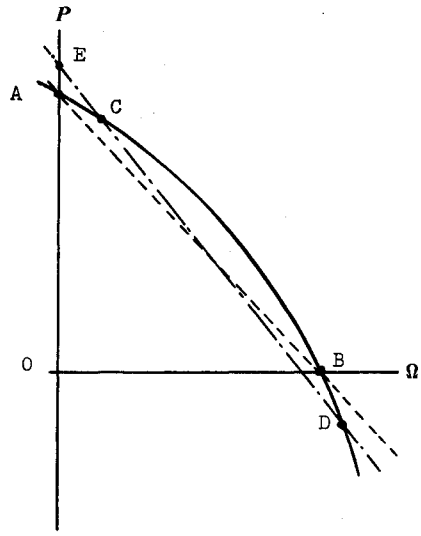

Fig. 1 Fundamental eigencurve; sign convention: compressive axial load is positive (——— = exact curve, — — — = straight-line approximation, — · — · — = another straight-line approximation, OA = exact buckling load, OE = approximate buckling load).

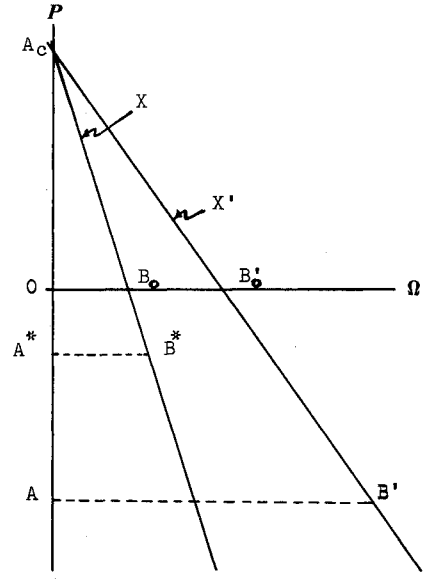

Fig. 2 Fundamental eigencurves of structures X and X' ($OA = P$, $OA^* = P^*$, $OA_C = P_C$, $OB_0 = \Omega_0$, $OB_0' = \Omega_0'$, $AB' = \Omega'$, $A^*B^* = \Omega^*$).

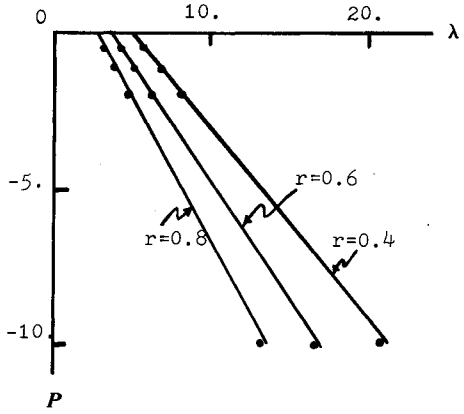

Fig. 3 Comparison of results.

effect of changes on mass distributions and axial loads, engineers would be more inclined to study the effect of mass distributions and axial loads and design more economical structural components and systems. A very simple method of calculating the fundamental frequencies of structures subjected to axial loads is presented in this Note.

Mathematical Formulation

Consider a structure defined by its stiffness distribution $S(x,y,z)$, mass distribution $\mu(x,y,z)$, and axial load P, where x, y, z are the spatial coordinates. The structure could be a beam, plate, or shell. A graph of the axial load P vs the square of the fundamental frequency ($\Omega = \omega^2$) is called the fundamental eigencurve. A sample fundamental eigencurve is shown in Fig. 1. Point B represents the fundamental frequency at zero axial load ($OB = \Omega_0$), and point A represents a fundamental frequency of zero. The axial load corresponding to a zero fundamental frequency is the buckling load of the structure ($OA = P_c$).

A straight line is a good approximation of the fundamental eigencurve. Straight-line approximations of the fundamental eigencurve may be obtained by joining any two points on the fundamental eigencurve (for example, points A and B or points C and D in Fig. 1), or by drawing a tangent to the fundamental eigencurve at any point on the curve; the popular Rayleigh's method for computing buckling loads is, in fact, one such straight-line approximation.

Consider two structures X and X'. Both structures have the same stiffness distribution $S(x,y,z)$, but their mass distributions are different. Let the mass distributions of X and X' be $\mu(x,y,z)$ and $\mu'(x,y,z)$, respectively. The two structures will have different fundamental frequencies at zero axial loads since they have different mass distributions. Let the square of the fundamental frequencies of structures X and X' at zero axial load be Ω_0 and Ω_0', respectively. These fundamental frequency points are denoted by B_0 and B_0', respectively, in Fig. 2 ($OB_0 = \Omega_0$, $OB_0' = \Omega_0'$).

Both structures have the same buckling load since they have the same stiffness distribution. If we know the fundamental frequencies of structure X at zero axial load and also at a nonzero axial load $P = P^*$, then a straight-line approximation of the fundamental eigencurve of structure X can be drawn (see Fig. 2). Let the square of the fundamental frequency of structure X at $P = P^*$ be Ω^*, and let that point be represented by B^* in Fig. 2 ($OA^* = P^*$, $A^*B^* = \Omega^*$). The intercept of the foregoing straight-line eigencurve with the P axis provides an approximate value for the buckling load of structure X. Let this point be denoted by A_C in Fig. 2 ($OA_C = P_C$). A straight-line approximation of the fundamental eigencurve of structure X' can be drawn by joining A_C and B_0' since both structures X and X' have the same critical load.

Now that we have established the fundamental eigencurve of structure X', the fundamental frequencies of structure X' at any axial load can be determined directly from this curve. For example, the square of the fundamental frequency of structure X' at an axial load P (denoted by point A in Fig. 2; $OA = P$) is given by the point B' ($AB' = \Omega'$), where Ω' is the square of the fundamental frequency of structure X' at an axial load equal to P.

By applying properties of similar triangles to the various triangles in Fig. 2, we get

$$AB' = OB_0' + \frac{OA}{OA^*}\frac{OB_0'}{OB_0}(A^*B^* - OB_0) \tag{1}$$

The foregoing equation may be written in terms of frequencies and axial loads as follows:

$$\Omega' = \Omega_0' + \frac{P}{P^*}\frac{\Omega_0'}{\Omega_0}(\Omega^* - \Omega_0) \tag{2}$$

Table 1 Comparison of results

			Square of the fundamental frequency, λ'		
r	λ_0'	p	Eq. (2)	Exact[2]	% Error
0.4	4.69	− 0.5	5.61	5.53	− 1.43
		− 1.0	6.52	6.37	− 2.30
		− 2.0	8.33	8.05	− 3.36
		− 10.0	21.85	21.48	− 1.69
0.6	3.57	− 0.5	4.28	4.21	− 1.64
		− 1.0	4.98	4.85	− 2.61
		− 2.0	6.36	6.13	− 3.62
		− 10.0	16.85	16.35	− 2.97
0.8	2.89	− 0.5	3.46	3.41	− 1.45
		− 1.0	4.03	3.92	− 2.73
		− 2.0	5.14	4.96	− 3.50
		− 10.0	13.70	13.24	− 3.36

where

Ω_0', Ω' = square of the fundamental frequency of structure X' at zero axial load and an axial load P, respectively
Ω_0, Ω^* = square of the fundamental frequency of structure X at zero axial load and an axial load P^*, respectively.

The practical implication and use of Eq. (2) are as follows. If we are interested in studying the effect of changes in mass distributions at various levels of axial loads, all that is needed are 1) the fundamental frequencies of a basic mass-distribution case (structure X) at zero and a nonzero axial load, and 2) the fundamental frequency of the mass distribution of interest (structure X') at zero axial load. Generally, a uniform mass distribution may be used as the basic mass-distribution case (structure X). Fundamental frequencies of such structures (beams, plates, shells, etc. with a uniform mass distribution) may be readily available in literature. If the structure is of a more complex nature, these two frequencies may be obtained by analysis or testing.

Numerical Results

Takahashi[2] presents a series of numerical results for axially loaded cantilever beams with nonuniform mass distributions (uniform mass plus a concentrated mass at the free end). His results are based on the numerical solution of the exact transcendental equation for the fundamental frequency.

The length of the cantilever beam is L, uniform mass is m per unit length, concentrated mass is M, and the axial load is P (compression is positive and tension negative). The fundamental frequency of lateral vibration is ω. The following nondimensional parameters are used: $p = (PL^2/EI)$, $r = (M/mL)$, and $\lambda = (mL^4/EI)\omega^2 = (mL^4/EI)\Omega$. Similarly, λ_0, λ^*, λ_0', and λ' are the nondimensional counterparts of Ω_0, Ω^*, Ω_0', and Ω', respectively.

When the mass ratio $r = 0$, we have the uniform mass-distribution case, which will be used as the basic mass-distribution case (structure X). We need two frequencies for this uniform mass-distribution case: one at zero axial load and another at a nonzero axial load; from Ref. 2, we have $\lambda_0 = 12.36$ at $p = 0$ and $\lambda^* = 21.21$ at $p = p^* = 2.0$. The mass distribution is varied by changing the mass ratio r. The square of the nondimensional fundamental frequency (λ_0') for the specific value of r, at zero axial load, is computed by a numerical solution of the frequency equation.

Fundamental frequencies at any nonzero axial load are calculated using Eq. (2); this computation (hand calculation) takes only a few seconds. Frequencies thus computed are compared against Takahashi's exact results[2] in Table 1. The accuracy of Eq. (2) is extremely good.

The results presented in Table 1 are plotted in Fig. 3. The straight lines represent the approximate solution provided by Eq. (2). The exact results from Ref. 2 are indicated by dots. All the exact results fall almost on top of or very close to the straight lines.

Concluding Remarks

A simple method of computing fundamental frequencies of axially loaded structures is presented. The excellent accuracy of the method is illustrated by applying it to an axially loaded cantilever beam with nonuniform mass distribution. The method is equally applicable to beams, stiffened or unstiffened plates, and stiffened or unstiffened shells with nonuniform stiffness distributions, complex geometries, and complex boundary conditions.

References

[1]Sundararajan, C., "Bounds for the Critical Load of Certain Elastic Systems Under Follower Forces," *AIAA Journal*, Vol. 14, No. 5, 1976, pp. 690–692.

[2]Takahashi, K., "Further Results on a Vibrating Beam with a Mass and Spring at the End Subjected to Axial Force," *Journal of Sound and Vibration*, Vol. 84, 1982, pp. 593, 594.

Effect of Transverse Shear Deformation on Imperfection Sensitivity of Cylindrical Panels

Gerald A. Cohen*
Structures Research Associates, Laguna Beach, California 92652

Introduction

Hui and Du[1] analyzed the initial postbuckling behavior of boron-epoxy antisymmetric cross-ply cylindrical panels under shear loading. The panels are assumed to be long enough to ignore the effect of the boundary conditions at the two curved edges.

For structures with unique symmetrical buckling modes, initial postbuckling and sensitivity to geometric imperfections are essentially determined by Koiter's second postbuckling coefficient b. Briefly, if $b > 0$, the structure can carry postbuckling loads in excess of the critical load, whereas if $b < 0$, the structure is imperfection sensitive and will fail at a load below the critical load.

In Ref. 1, the calculation of the critical load and postbuckling coefficient is based on the Donnell shell theory, and the results are correlated with the curvature parameter

$$\Theta = B/(Rh)^{1/2}$$

where B is the curved panel width, R its radius of curvature, and h its thickness. Within the assumptions of the Donnell theory, the results are independent of the radius-to-thickness ratio R/h.

Cohen and Haftka[2] reanalyzed the two-layer clamped panels of Ref. 1 using the code FASOR (field analysis of shells of revolution). This analysis, which is based on classical shell theory using a large radius toroidal model with $R/h = 100$ (Fig. 1), predicts imperfection-insensitive panels ($b > 0$) over the range $0 \leq \Theta \leq 8$.

The purpose of this Note is to re-examine these panels considering the effect of radius-to-thickness ratio using both clas-

Received May 9, 1991; revision received July 8, 1991; accepted for publication July 8, 1991.

*President, P.O. Box 1348.